Journal Pre-proof

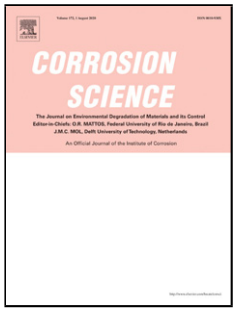

Y-Hf co-doped AlCoCrFeNi$_{2.1}$ eutectic high-entropy alloy with excellent oxidation and spallation resistance under thermal cycling conditions at 1100 °C and 1200 °C

Jie Lu, Han Zhang, Ling Li, Ying Chen, Xuanzhen Liu, Xiaofeng Zhao, Fangwei Guo

PII: S0010-938X(21)00281-X

DOI: https://doi.org/10.1016/j.corsci.2021.109515

Reference: CS 109515

To appear in: *Corrosion Science*

Received Date: 8 March 2021

Revised Date: 26 April 2021

Accepted Date: 27 April 2021

Please cite this article as: Lu J, Zhang H, Li L, Chen Y, Liu X, Zhao X, Guo F, Y-Hf co-doped AlCoCrFeNi$_{2.1}$ eutectic high-entropy alloy with excellent oxidation and spallation resistance under thermal cycling conditions at 1100 °C and 1200 °C, *Corrosion Science* (2021), doi: https://doi.org/10.1016/j.corsci.2021.109515

Y-Hf co-doped $AlCoCrFeNi_{2.1}$ eutectic high-entropy alloy with excellent oxidation and spallation resistance under thermal cycling conditions at 1100 °C and 1200 °C

Jie Lu [a], Han Zhang [a], Ling Li [a], Ying Chen [b], Xuanzhen Liu [a], Xiaofeng Zhao [a,*], Fangwei Guo [a]

[a]Shanghai Key Laboratory of Advanced High-Temperature Materials and Precision Forming, School of Materials Science and Engineering, Shanghai Jiao Tong University, Shanghai, 200240, China

[b]School of Materials, The University of Manchester, Manchester M13 9PL, United Kingdom

Corresponding author: Xiaofeng Zhao (xiaofengzhao@sjtu.edu.cn)

Graphical Abstract

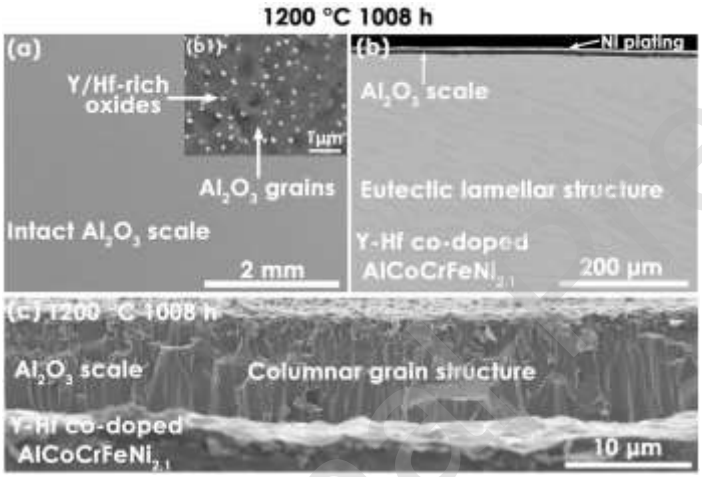

Highlights

- The oxidation rates of Y-Hf co-doped $AlCoCrFeNi_{2.1}$ EHEA at 1100 °C and 1200 °C are much lower than those of NiCoCrAlYHf alloy.
- The Y-Hf co-doped $AlCoCrFeNi_{2.1}$ EHEA exhibits a strong scale interfacial adhesion at 1100 °C and 1200 °C.
- The Y-Hf co-doped $AlCoCrFeNi_{2.1}$ EHEA shows a highly structural stability after prolonged oxidation at 1100 °C and 1200 °C.
- The Y-Hf co-doped $AlCoCrFeNi_{2.1}$ EHEA might be a promising candidate as the oxidation-protective overlay coating material.

Abstract

The oxidation behavior of $AlCoCrFeNi_{2.1}$ eutectic high-entropy alloy (EHEA) with Y-Hf co-doping under thermal cycling conditions at 1100 °C and 1200 °C is studied in comparison to the conventional NiCoCrAlYHf alloy (CNA). The oxidation rates of EHEA at two temperatures are much lower than those of CNA. Additionally, the resistance to Al_2O_3 scale spallation for the EHEA is much superior to that for the CNA. It is well demonstrated that increasing the interfacial toughness is more beneficial to improve the scale spallation resistance in comparison to the decrease in oxidation rate.

Keywords: High-entropy alloy; Eutectic structure; Oxidation; High-temperature; thermal cycling

Introduction

High-entropy alloys (HEAs) have been intensively developed and studied due to their unique structure and excellent physical properties [1-5]. Distinguishing from the conventional alloys with one or two principal matrix elements plus minor additions of other elements, HEAs contain multiple principal elements [3, 5, 6], which is first proposed by Yeh and Cantor et al. [7,8] in 2004. At present, the single-phase face-centered cubic (FCC) HEAs or body-centered cubic (BCC) HEAs have become the most studied HEAs systems. However, the single-phase FCC HEAs are commonly low strength [1], while the single-phase BCC HEAs are always too brittle [9]. It is still a main challenge to realize an appropriate match of strength and ductility for a single-phase HEA. In addition, engineering applications of a single-phase HEA are always difficult to be achieved, because of their poor cast-ability and common compositional segregation [10].

To break the shortcomings mentioned above for a single-phase HEA, the $AlCoCrFeNi_{2.1}$ eutectic high-entropy alloy (EHEA) with good cast-ability has been proposed in 2014 [11], which achieves an almost perfect balance of strength and ductility and thus attracts extensive attention [10, 12, 13]. It should be specially mentioned that the $AlCoCrFeNi_{2.1}$ EHEA shows an enormous potential in high-temperature applications. First, the eutectic structure originates from an isothermal transformation without a solidification-temperature range, and thus the near-equilibrium solidification structure is beneficial to ensure the high-temperature stability as high as their reaction temperatures. Second,

low-energy phase boundary in the eutectic solidification structure can increase their kinetic resistance to the structural degradation [11, 14, 15]. Third, the sluggish diffusion effect in the HEA deriving from the fluctuant lattice potential energy might be very important to contribute to outstanding creep-resistant performance at high temperatures, even if this effect has not yet been probed directly [16].

Before considering the high-temperature applications of $AlCoCrFeNi_{2.1}$ EHEA, its oxidation resistance at elevated temperatures should be first evaluated. In our recent work [17], it has been well demonstrated that the reactive element Y-doped $AlCoCrFeNi_{2.1}$ EHEA exhibits remarkable oxidation performance in the isothermal oxidation manner via forming continuous, adherent and slowly growing Al_2O_3 scale at 1000 °C and 1100 °C. The superior oxidation performance with highly stable eutectic structure makes the $AlCoCrFeNi_{2.1}$ EHEA with reactive elements doping show huge potential in high-temperature applications. Generally, the isothermal oxidation test is merely utilized to investigate the oxidation mechanism of alloy, but it is difficult to reflect the interfacial adhesion and spallation resistance of Al_2O_3 scale, which requires a comprehensive and in-depth study.

In this contribution, the cyclic oxidation tests at 1100 °C and 1200 °C are performed to evaluate the interfacial adhesion and spallation resistance of Al_2O_3 scale growing on the $AlCoCrFeNi_{2.1}$ EHEA with Y-Hf co-doping in this study. The Y and Hf are the most common doping elements for the conventional Al_2O_3-forming alloys (e.g., NiCoCrAlYHf and FeCrAlYHf), while the doping concentration of Y and Hf is 0.025 at% referring to the oxidation resistant FeCrAlYHf alloy [18, 19]. In addition, the test temperature of 1200 °C is fairly high for evaluating the oxidation performance under thermal cycling conditions, which can further reflect the cyclic oxidation resistance of $AlCoCrFeNi_{2.1}$ EHEA. In addition, the conventional Al_2O_3-forming NiCoCrAlYHf alloy was also fabricated as a counterpart to the Y-Hf co-doped $AlCoCrFeNi_{2.1}$ EHEA. The structure of Al_2O_3 scale and underlying alloy substrate, growth rate of Al_2O_3 scale, the residual stress in Al_2O_3 scale and the interfacial S segregation are characterized to clarify the oxidation and spallation mechanisms of Y-Hf co-doped $AlCoCrFeNi_{2.1}$ EHEA at 1100 °C and 1200 °C.

2 Materials and method

2.1 Alloy preparation

Two alloys according to the nominal composition of $AlCoCrFeNi_{2.1}$ (Ni-

18.6Co-17.6Fe-16.4Cr-8.5Al, in wt.%) and NiCoCrAl (Ni-22.8Co-16.7Cr-12.3Al, in wt.%) with the doping concentration of 0.025 at.% reactive elements Y and Hf (≥ 99.9 wt.%) were fabricated using arc-melting under a Ti-gettered high-purity argon atmosphere and subsequently solidified in a water-cooled copper mold with the size of 30 mm (width) × 50 mm (length) × 10 mm (thickness). Each ingot has a weight of about 100 g. To obtain high quality melt with homogeneous chemical composition, the ingots were re-melted at least four times. Finally, two ingots were heat treated for 2 h at 1100 °C in a tube furnace under vacuum condition (≤10^{-5} Pa) to achieve a further homogenization. The Y-Hf co-doped $AlCoCrFeNi_{2.1}$ eutectic high-entropy alloy was designated as ***EHEA,*** while the conventional NiCoCrAlYHf alloy was designated as ***CNA.***

2.2 Cyclic oxidation test

The rectangular plates were first cut using electro-discharge machining and were subsequently processed in the size of 10 mm × 10 mm × 3 mm using a precise cutting machine. The sample surface for oxidation test were mechanically ground and polished according to the standard metallographic approaches, while the sample edge was chamfered to avoid the edge effect. The samples were ultrasonically cleaned using acetone for 10 min before cyclic oxidation test. The samples were put in the corundum crucibles and the sample surface of 10 mm × 10 mm was oxidized to study the oxidation behavior. The cyclic oxidation tests were performed in an automatically controlled circulating heating furnace at atmosphere environment. Each cycle consists of 12 h heating at 1100 °C or 1200 °C and 10 min cooling via the fan-assisting cooling to room temperature.

2.3 Samples characterization

The scanning electron microscopy (SEM, Mira3, Tescan) coupled with energy dispersive X-ray spectroscopy (EDS, Oxford Instruments) was utilized to determine the microstructure and phase constitutions of two alloys and oxide scale formed on the two alloys. The analytical scanning transmission electron microscope (STEM, Talos F200X G2, Thermo Fisher Scientific, USA) combined with energy-dispersive X-ray spectroscopy (EDS) system was used to identify the chemical composition. The microscope was operated at 200 kV. The TEM lamella was prepared using the focused ion beam (FIB, GAIA3, Tescan, Czech Republic). The semi-quantitative depth profile of corresponding elements from scale surface to alloy substrate was characterized using radiofrequency glow discharge optical emission spectroscopy (GD-

OES, GDA750HP, Spectruma Analytik GmbH, Germany). The residual stress in Al_2O_3 scale was measured and calculated by the frequency shift of the photoluminescence piezospectroscopy (PLPS) from Cr^{3+} in Al_2O_3 scale under a green 532 nm Nd:YAG laser. The measurement was conducted at room temperature in ambient air using a confocal Raman microprobe (LabRAM HR, Horiba Jobin Yvon, France).

3. Results

3.1 Microstructure of EHEA

Fig. 1 shows the structure of EHEA. A typical alternating lamellar morphology can be clearly observed in Fig. 1a and b. The bright and dark phases are respectively the $L1_2$-structured phase (γ') and the B2-structured phase (β), according to our previous work [17] and other literature reports [10-12, 20]. The ultra-fine two phases with the average phase width less than 500 nm are uniformly distributed in the lamellar structure. The HAADF STEM image combined with the elemental maps suggests that the γ' phase is CoCrFe-rich and the β phase is NiAl-rich (Fig. 1c and d). The chemical composition of γ' and β is respectively identified to be $Al_{9.4}Co_{19.6}Cr_{19.2}Fe_{19.9}Ni_{31.9}$ and $Al_{29.2}Co_{12.5}Cr_{4.7}Fe_{9.7}Ni_{43.9}$ through the STEM-EDS point analysis. In addition, no Y/Hf-rich intermetallic compounds precipitate from phase/grain boundaries due to the extremely low concentration of Y and Hf doping (0.025 at.%) and the full solution of Y and Hf into the alloy matrix.

3.2 Oxidation and spallation resistance of EHEA at 1100 °C and 1200 °C

Fig. 2 shows surface and cross-sectional morphology of the EHEA after 1008 h cyclic oxidation at 1100 °C and 1200 °C. At either oxidation test temperature, no any Al_2O_3 scale spallation can be found and the Al_2O_3 scale shows outstanding adhesive property with the alloy substrate (Fig 2a and d). The localized amplification of scale surface suggests that the Y/Hf-rich oxides are uniformly distributed at the triple junctions of Al_2O_3 grain boundaries, which also reflects the homogeneous distribution of Y and Hf in the alloy (Fig. 2a1 and d1). A homogeneous and continuous Al_2O_3 scale develops at the alloy surface, while no interfacial imperfections can be seen at the scale/alloy interface, ensuring a strong interfacial bonding (Fig. 2b and e). Additionally, the lamellar structure consisting of γ' and β phases is still obvious except for the increasing phase size after 1008 h oxidation at 1100 °C and1200 °C, demonstrating its excellent structure stability up to 1200 °C (Fig. 2b and e). The thickness of Al_2O_3 scale reaches 4.7 ± 0.4 μm after 1008 h cyclic oxidation at 1100 °C, while the thickness of Al_2O_3 scale after 1008 h

cyclic oxidation at 1200 °C is two times higher than that at 1100 °C, attaining 10.2 ± 0.5 μm (Fig. 2c and f). The Al_2O_3 scale is almost absolute columnar grain structure and no equiaxed grains forms during the scale growth. The simultaneous diffusion of aluminum and oxygen along scale grain boundaries forms equiaxed grains and the inward oxygen diffusion forms columnar grains [21, 22]. This result demonstrates that the scale thickening derives from the reaction of aluminum and oxygen at scale/alloy interface, thus the scale grows by inward grain boundary diffusion of oxygen (Fig. 2g).

To emphasize the superiority of EHEA to the oxidation and spallation resistance of Al_2O_3 scale at 1100 °C and 1200 °C, Fig. 3 shows the surface and cross-sectional morphology of the Al_2O_3-forming CNA after cyclic oxidation at 1100 °C and 1200 °C. As presented in Fig. 3a, the Al_2O_3 scale bears severe spallation after merely 720 h cyclic oxidation at 1100 °C, and the spallation mainly occurs along scale/alloy interface. Additionally, the thickness of Al_2O_3 scale is about 5.5 ± 0.4 μm after 720 h oxidation at1100 °C, which is even higher than that of EHEA after 1008 h cyclic oxidation at 1100 °C (Fig. 3b). In the case of cyclic oxidation at 1200 °C, the Al_2O_3 scale suffers from destructive spallation after a shorter oxidation time (504 h), as shown in Fig. 3c. Differing from the mode of scale spallation at 1100 °C, plenty of interfacial imperfections enriched with Y/Hf-rich oxides, also termed as oxide intrusions [23], occur at the spalled interface (Fig. 3c, c1 and d). In addition, the scale thickness away from the interfacial imperfections reaches 8.8 ± 0.7 μm (Fig. 3d). It can be clearly observed that the cracks nucleate surrounding the interfacial imperfections (Fig. 3d). The interfacial imperfections play an important role in facilitating scale spallation, which will be discussed in later section. The growth of Al_2O_3 scale formed on the CNA is also controlled by inward grain boundary diffusion of oxygen, resulting from the almost identical columnar grain structure of scale to that formed on the EHEA (Fig. 2g and 3e).

Through the comparison of oxidation and spallation resistance in the cyclic oxidation manner between EHEA and CNA at 1100 °C and 1200 °C, it is clearly demonstrated that EHEA exhibits a much stronger resistance to the scale spallation at 1100 °C and 1200 °C, which is significantly superior to that of CNA.

3.3 Oxidation kinetics

According the scale structure in Fig. 2g and 3e, the growth of Al_2O_3 scale formed on two alloys is predominantly dominated by inward grain boundary diffusion of oxygen at 1100 °C and 1200 °C. According to the classical diffusion-controlled oxidation theory [24], the thickening

process of Al_2O_3 scale should comply with a parabolic law at 1100 °C and 1200 °C:

$$h^2 = k_h t \quad (1)$$

where h, t and k_h are the thickness of Al_2O_3 scale, the oxidation time and the oxidation rate constant, respectively.

Fig. 4 shows the evolution of Al_2O_3 scale thickness as a function of oxidation time at 1100 °C and 1200 °C for the EHEA and the CNA. The oxidation rate constant at 1100 °C is calculated to be 6.0×10^{-14} cm^2/s for the EHEA through the linear fitting, which is 45% lower than that (1.1×10^{-13} cm^2/s) for the CNA at 1100 °C. Additionally, the oxidation rate constant at 1200 °C is 2.7×10^{-13} cm^2/s for the EHEA, which is 34% lower than that (4.1×10^{-13} cm^2/s) for the CNA at 1200 °C. The oxidation rate constant of CNA at 1100 °C is lower than that (3×10^{-13} cm^2/s~16×10^{-13} cm^2/s) of a CoNiCrAlY coating at 1100 °C, reported by Evans and Taylor [25]. It is likely that the Y-Hf co-doping is beneficial to lower the oxidation rate. It should be also mentioned that the oxidation rate of EHEA with Y-Hf co-doping at 1100 °C is 88% lower than that of EHEA with single Y-doping at 1100 °C [17]. The synergistic effect of Y-Hf co-doping on the lowering the oxidation rates of EHEA and CNA will be reported in our future work, which is not the scope of this study. Generally, the oxidation rates of the EHEA at 1100 °C and 1200 °C are much lower than those of CNA at 1100 °C and 1200 °C.

To further highlight the slow oxidation rates of the EHEA at 1100 °C and 1200 °C, the oxidation rate constants are compared with that of the ultra oxidation resistant NiAlHf alloy [26]. First, the oxidation rate constants calculated from the Al_2O_3 scale thickness for the EHEA are transformed into those on account of the mass gain [25, 27]:

$$k_p = \left(\frac{3M_O\rho_{Al_2O_3}}{M_{Al_2O_3}}\right)^2 k_h \quad (2)$$

where M_O (16 g/mol) and $M_{Al_2O_3}$ (102 g/mol) are molar mass of O and Al_2O_3, respectively. $\rho_{Al_2O_3}$ (3.98 g/cm^3) is the density of Al_2O_3.

Based on the equation (2), the transformed oxidation rate constants of EHEA at 1100 °C and 1200 °C are 2.1×10^{-13} $g^2\ cm^{-4}\ s^{-1}$ and 9.5×10^{-13} $g^2\ cm^{-4}\ s^{-1}$, respectively. According the results reported by Pint et al. [18, 26], the oxidation rate constants of NiAlHf at 1100 °C and 1200 °C are respectively about 1.6×10^{-13} $g^2\ cm^{-4}\ s^{-1}$ and 1.0×10^{-12} $g^2\ cm^{-4}\ s^{-1}$, while the oxidation rate constant of commercial FeCrAlYHf at 1200 °C is 3.5×10^{-12} $g^2\ cm^{-4}\ s^{-1}$. Thus, the oxidation rates of EHEA at 1100 °C and

1200 °C are substantially comparable to those of NiAlHf alloy, while its oxidation rate at 1200 °C is lower than that of FeCrAlYHf.

However, the B2 structured NiAlHf is intrinsically brittle, thus limiting its engineering applications [28]. In addition, the addition of Cr element into NiAlHf is necessary to assure its hot-corrosion resistance, but the Cr element is detrimental to the outstanding oxidation performance of NiAlHf, because the Cr addition will increase its oxidation rate and weaken its scale adhesion dramatically [29-32]. Differing from the NiAlHf alloy, the Cr content (16.4 at.%) in the EHEA is extremely higher, which should be enough to confer its hot-corrosion resistance.

4. Discussion

It has been well demonstrated in this work that the EHEA exhibit ultra-strong oxidation and spallation resistance in the cyclic oxidation manner at 1100 °C and 1200 °C in comparison to the CNA. Actually, the underlying mechanism for a lower oxidation rate of EHEA with respect to the CNA at an identical oxidation test temperature is not very clear, since the Al_2O_3 scale growth of two alloys are both dominated by inward grain boundary diffusion of oxygen judged by the typical columnar grain structure of scale (Fig. 2g and 3e) [21, 33]. It is speculated that the effect of reactive elements doping in a different alloy matrix on lowering the oxidation rate is fairly different. For instance, the oxidation rates of NiAlHf and FeCrAlY are much lower than that of NiCoCrAlY alloy at a same oxidation temperature [26, 34, 35]. Moreover, the synergetic effect of Y-Hf co-doping on the scale growth in a different alloy matrix should be more complicated, which requires a further work. In this section, it will be focused to discuss the mechanism for the much stronger spallation resistance of Al_2O_3 scale at 1100 °C and 1200 °C for the EHEA compared with the CNA.

It is well known that two contributing factors determine the scale spallation: one is the elastic strain energy stored in the G, also termed as driving force for scale delamination, which is in proportion to the scale thickness h_{ox}, and the square of residual stress in scale σ; the other one is the interfacial toughness G_c, which degrades due to the interfacial imperfections growth and the interfacial S segregation. Once the driving force for scale delamination G exceeds the interfacial toughness G_c, the scale will detach from the interface [34, 36, 37]:

$$G = \frac{(1-v_{ox}^2)\sigma^2 h_{ox}}{2E_{ox}} \qquad (3)$$

where E_{ox} and v_{ox} are Young' modulus and Poisson' ratio of Al_2O_3 scale, respectively.

4.1 Driving force for scale delamination

The residual stress in Al_2O_3 scale σ is an important component of the driving force for scale delamination based on the Equation (3), which can be measured using PLPS technique, by [34, 38]

$$\Delta v = 5.07\sigma \quad (4)$$

where Δv is the peak shift of R2 line collected from the Al_2O_3 scale with respect to the stress-free sapphire. The residual stress in Al_2O_3 scale predominantly consists of the thermal mismatch stress between Al_2O_3 scale and alloy upon cooling from high temperature to room temperature and growth stress deriving from the lateral scale growth [38-40]. The evolution of residual stress in the Al_2O_3 scale with the accumulated oxidation time for two alloys at 1100 °C and 1200 °C is displayed in Fig. 5. First, the original stress level can represent the actual stress before relaxation, and the stress values are substantially same for two alloys, which are about -5.8 GPa and -7.2 GPa at 1100 °C and 1200 °C, respectively. Second, for the CNA after 240 h oxidation at 1100 °C, the stress begins to decrease quickly, and then falls to about -2.6 GPa after 720 h oxidation, while the stress declines at a faster speed at 1200 °C, and eventually drops to about -2.8 GPa after 504 h oxidation. The fast stress relaxation in the Al_2O_3 scale for the CNA suggests that the interfacial cracks or detachments have already nucleated before the scale spallation (Fig. 3d). Finally, the EHEA keeps a stable stress level up to oxidation time of 1008 h at 1100 °C and 1200 °C, which also reflects a stable interfacial structure with a good interfacial adhesion.

Since the original residual stress in Al_2O_3 scale is comparable for two alloys after oxidation at 1100 °C and 1200 °C, the residual stress is not the dominating factor for contributing to the difference in spallation resistance of scale. A higher oxidation rate for the CNA after oxidation at 1100 °C and 1200 °C signifies a higher driving force for scale delamination under the circumstance of an almost equal residual stress in Al_2O_3 scale for two alloys according to the Equation (3).

4.2 Interfacial toughness

The interfacial toughness is predominantly determined by the interfacial S segregation and interfacial imperfections growth [23, 34, 41]. In our previous works [34, 42], it has been well affirmed that the impurity S predominantly segregates at scale/metal interface after thermal oxidation exposure for the NiCoCrAlY or NiCoCrAlYHf alloys, since the inhomogeneous distribution of Y or Hf in the alloy resulting

from the intrinsic phase structure of alloy will weaken the reactive elements effect. The S segregation to scale/alloy interface can decline the interfacial toughness rapidly [43-46]. Meanwhile, the fine phase size of alloy can facilitate the homogeneous distribution of Y or Hf, thus suppressing the interfacial S segregation [42]. For the EHEA in this work, its phase structure is also extremely fine with a phase width of less than 500 nm (Fig.1).

To reveal the S segregation at scale/alloy interface for the oxidized EHEA, the elemental profile along the depth direction of Al_2O_3 scale was obtained using GD-OES [47]. Fig. 6 shows the change of concentration of corresponding elements with the sputtering depth for the EHEA after oxidation for 1008 h at 1200 °C obtained using GD-OES. The sputtering depth reaching scale/metal interface is about 10.8 μm, which is substantially consistent to the Al_2O_3 scale thickness for EHEA after oxidation for 1008 h at 1200 °C (10.2 ± 0.5 μm). A high S concentration can be observed near the scale surface. Instead, the interfacial S segregation is well suppressed, probably resulting from the fine phase structure of EHEA. In short, interfacial segregation of high concentration of S is suppressed for the EHEA, and thus increase the interfacial toughness effectively.

It should be noted that the interfacial imperfections enriched with Y/Hf-rich oxides grow at interface for the CNA after oxidation at 1200 °C, which are not seen after oxidation at 1100 °C (Fig. 3a-d). This result indicates that the formation of interfacial imperfections does not derive from the over-doping of Y and Hf [48]. First, an extremely high temperature at 1200 °C will increase the diffusion rate of Y and Hf to scale/alloy interface along the phase boundaries. Second, the γ and β phases coarsen quickly at 1200 °C, thus reducing the distribution locations of Y and Hf in the alloy substrate (Fig. 3d). The two factors mentioned above could lead to the local enrichment of Y and Hf after the prolonged oxidation, and thus facilitate the formation of interfacial imperfections [23]. However, the EHEA exhibits a much finer phase structure after 1008 h oxidation at 1200 °C compared with the CNA after 504 h oxidation at 1200 °C (Fig. 2d and 3d). A higher phase boundary density for the EHEA leads to the homogeneous distribution of Y and Hf in the alloy substrate, and thus suppresses the nucleation and coarsening of interfacial imperfections. The interfacial imperfections cause the local stress concentration easily, which nucleates the cracks surrounding the imperfections and causes a further decrease in interfacial toughness (Fig. 3d).

4.3 Understanding the spallation resistance of Al_2O_3 scale

Take the discussion mentioned above into consideration: (1) as proposed by Jackson et al.[37], the tendency for scale delamination is directly related to the driving force for scale delamination, which is proportional to the scale thickness, and thus parabolically increases with the oxidation time, t; (2) the interfacial S segregation causes a quick decline of interfacial toughness for CNA after oxidation at 1100 °C and 1200 °C, while the interfacial toughness declines at a faster rate at 1200 °C due to the formation of interfacial imperfections (oxidation intrusions) [43-46]; (3) the interfacial toughness decreases at a low rate for the EHEA, since the S concentration at scale/metal interface is extremely low; (4) for the EHEA, the decreasing rate in interfacial toughness in the initial oxidation stage should be higher at 1200 °C than that at 1100 °C, resulting from a faster rate of interfacial S segregation even though a low S concentration at interface. Fig. 7 shows the schematic diagram, reflecting the evolution tendency of driving force for scale delamination and interfacial toughness for two alloys with the accumulated oxidation time at 1100 °C and 1200 °C. The intersecting point of these two curves represents the time to scale delamination. The higher interfacial toughness combined with the lower driving force for scale delamination for the EHEA lead to the ultra-strong scale spallation resistance at 1100 °C and 1200 °C, compared with the CNA.

Another important point should be noted and discussed. The CNA exhibits the severe scale spallation after 504 h oxidation at 1200 °C, while the scale thickness reaches 8.8 ± 0.7 μm (Fig. 3b, d and Fig. 4). However, when the scale thickness attains 10.2 ± 0.5 μm after 1008 h oxidation at 1200 °C for the EHEA, the scale is still well bonded with the alloy (Fig. 2d-f and Fig. 4). In short, a higher driving force for the scale delamination (higher scale thickness) for the EHEA in comparison to the CNA does not lead to the scale spallation. Therefore, a higher interfacial toughness for the EHEA resulting from the well inhibiting effect of interfacial S segregation and interfacial imperfections growth plays a more important role in improving the spallation resistance of scale. This result also provides a good guidance for designing the oxidation and spallation resistant high-temperature alloys in the future: compared with the lower oxidation rate, improving the interfacial toughness could be more effective for strengthening the spallation resistance of scale.

5. Conclusions

In this study, the oxidation and spallation resistance of Y-Hf co-doped $AlCoCrFeNi_{2.1}$ EHEA (EHEA)under thermal cycling conditions at 1100 °C and 1200 °C were investigated via a detailed comparison to the conventional NiCoCrAlYHf alloy (CNA). The following conclusions can be drawn:

(1) The EHEA consists of ultra-fine lamellar γ' and β phases with an average phase width less than 500 nm. In addition, the two-phase structure is highly stable except for the increase in phase size during the prolonged oxidation.

(2) The oxidation rates at 1100 °C and 1200 °C for the EHEA are much lower compared with those of CNA and even comparable to those of ultra oxidation resistant NiAlHf alloy. The slow Al_2O_3 scale growth rate is attributed to the synergistic effect of Y-Hf co-doping on the scale growth for the EHEA, which requires a further work.

(3) The homogeneous and continuous Al_2O_3 scale with an imperfections-free scale/metal interface after the prolonged cyclic oxidation for the EHEA ensures a strong interfacial adhesion. Compared with the CNA, the ultra-strong resistance to scale spallation for the EHEA during the cyclic oxidation at 1100 °C and 1200 °C is ascribed to the low driving force for scale delamination and the high interfacial toughness.

(4) In comparison to a lower oxidation rate, increasing the interfacial toughness by suppressing the interfacial S segregation and the formation of interfacial imperfections could be more effective to improve the spallation resistance of scale for the EHEA. This result probably provides an approach for designing the oxidation and spallation resistant alloys for high-temperature applications in the future.

In summary, the outstanding oxidation performance and structural stability of EHEA at 1100 °C and 1200 °C makes this alloy show huge potential in high-temperature applications. This work is merely an initial exploration for the cyclic oxidation resistance of EHEA at 1100 °C and 1200 °C. In the future, more extensive works are required to achieve its high-temperature applications, including the synergistic effect of Y-Hf co-doping, the failure mechanism of Al_2O_3 scale, the mechanical properties at high temperatures, and so on.

Author statement

Jie Lu: Conceptualization, Data curation, Writing-Original draft preparation, Writing-Review & Editing. **Han Zhang and Ling Li:** Writing-

Review & Editing. **Xiaofeng Zhao:** Funding, Writing-Review & Editing. **Xuanzhen Liu**, **Ying Chen and Fangwei Guo:** Methodology, Formal analysis.

Declaration of interests

The authors declare that they have no known competing financial interests or personal relationships that could have appeared to influence the work reported in this paper.

Acknowledgement

This work was financially supported by National Natural Science Foundation of China (51971139) and National Major Science and Technology Project of China (2017-VI-0011-0083).

Data availability

The raw/processed data required to reproduce these findings can be shared upon reasonable requests.

References

[1] B. Gludovatz, A. Hohenwarter, D. Catoor, E.H. Chang, E.P. George, R.O. Ritchie, A fracture-resistant high-entropy alloy for cryogenic applications, Science 345(6201) (2014) 1153-1158.
[2] Z. Li, K.G. Pradeep, Y. Deng, D. Raabe, C.C. Tasan, Metastable high-entropy dual-phase alloys overcome the strength-ductility trade-off, Nature 534(7606) (2016) 227-30.
[3] D.B. Miracle, O.N. Senkov, A critical review of high entropy alloys and related concepts, Acta Mater. 122 (2017) 448-511.
[4] M.C. Gao, J.-W. Yeh, P.K. Liaw, Y. Zhang, High-Entropy Alloys Fundamentals and Applications, Springer International Publishing 2016.
[5] Y. Zhang, T.T. Zuo, Z. Tang, M.C. Gao, K.A. Dahmen, P.K. Liaw, Z.P. Lu, Microstructures and properties of high-entropy alloys, Prog. Mater. Sci. 61 (2014) 1-93.
[6] Y.F. Ye, Q. Wang, J. Lu, C.T. Liu, Y. Yang, High-entropy alloy: challenges and prospects, Mater. Today 19(6) (2016) 349-362.
[7] J.W. Yeh, S.K. Chen, S.J. Lin, J.Y. Gan, T.S. Chin, T.T. Shun, C.H. Tsau, S.Y. Chang, Nanostructured High-Entropy Alloys with Multiple Principal Elements: Novel Alloy Design Concepts and Outcomes, Adv. Eng. Mater. 6(5) (2004) 299-303.
[8] B. Cantor, I.T.H. Chang, P. Knight, A.J.B. Vincent, Microstructural development in equiatomic multicomponent alloys, Mater. Sci. Eng. A. 375-377 (2004) 213-218.
[9] Y. Zou, S. Maiti, W. Steurer, R. Spolenak, Size-dependent plasticity in an $Nb_{25}Mo_{25}Ta_{25}W_{25}$ refractory high-entropy alloy, Acta Mater. 65 (2014) 85-97.
[10] X. Gao, Y. Lu, B. Zhang, N. Liang, G. Wu, G. Sha, J. Liu, Y. Zhao, Microstructural origins of high strength and high ductility in an AlCoCrFeNi2.1 eutectic high-entropy alloy, Acta Mater. 141 (2017) 59-66.
[11] Y. Lu, Y. Dong, S. Guo, L. Jiang, H. Kang, T. Wang, B. Wen, Z. Wang, J. Jie, Z. Cao, H. Ruan, T. Li, A promising new class of high-temperature alloys: eutectic high-entropy alloys, Sci Rep 4 (2014) 6200.
[12] P. Shi, W. Ren, T. Zheng, Z. Ren, X. Hou, J. Peng, P. Hu, Y. Gao, Y. Zhong, P.K. Liaw, Enhanced strength-ductility synergy in ultrafine-grained eutectic high-entropy alloys by inheriting microstructural lamellae, Nat Commun 10(1) (2019) 489.
[13] I.S. Wani, T. Bhattacharjee, S. Sheikh, Y.P. Lu, S. Chatterjee, P.P. Bhattacharjee, S. Guo, N. Tsuji, Ultrafine-Grained $AlCoCrFeNi_{2.1}$Eutectic High-Entropy Alloy, Mater. Res. Lett. 4(3) (20 16) 174-179.
[14] M.E. Glicksman, Principles of Solidification: An Introduction to

Modern Casting and Crystal Growth Concepts, Springer, New York, NY, 2011.
[15] Y. Lu, Y. Dong, H. Jiang, Z. Wang, Z. Cao, S. Guo, T. Wang, T. Li, P.K. Liaw, Promising properties and future trend of eutectic high entropy alloys, Scr. Mater. 187 (2020) 202-209.
[16] K.Y. Tsai, M.H. Tsai, J.W. Yeh, Sluggish diffusion in Co–Cr–Fe–Mn–Ni high-entropy alloys, Acta Mater. 61(13) (2013) 4887-4897.
[17] J. Lu, H. Zhang, Y. Chen, L. Li, X. Liu, W. Xiao, N. Ni, X. Zhao, F. Guo, P. Xiao, Y-doped $AlCoCrFeNi_{2.1}$ eutectic high-entropy alloy with excellent oxidation resistance and structure stability at 1000°C and 1100°C, Corros. Sci.180 (2021).
[18] B.A. Pint, Optimization of Reactive-Element Additions to Improve Oxidation Performance of Alumina-Forming Alloys, J. Am. Ceram. Soc. 86(4) (2003) 686-695.
[19] K.A. Unocic, B.A. Pint, Characterization of the alumina scale formed on a commercial MCrAlYHfSi coating, Surf. Coat. Technol. 205 (2010) 1178-1182.
[20] I.S. Wani, T. Bhattacharjee, S. Sheikh, P.P. Bhattacharjee, S. Guo, N. Tsuji, Tailoring nanostructures and mechanical properties of AlCoCrFeNi2.1 eutectic high entropy alloy using thermo-mechanical processing, Mater. Sci. Eng. A. 675 (2016) 99-109.
[21] B.A. Pint, Experimental observations in support of the dynamic-segregation theory to explain the reactive-element effect, Oxid. Met. 45(1-2) (1996) 1-37.
[22] F.A. Golightly, F.H. Stott, G.C. Wood, The influence of yttrium additions on the oxide-scale adhesion to an iron-chromium-aluminum alloy, Oxid. Met. 10(3) (1976) 163-187.
[23] A.G. Evans, D.R. Mumm, J.W. Hutchinson, G.H. Meier, F.S. Pettit, Mechanisms controlling the durability of thermal barrier coatings, Prog. Mater. Sci. 46(5) (2001) 505-553.
[24] C. Wagner, Theoretical Analysis of the Diffusion Processes Determining the Oxidation Rate of Alloys, J. Electrochem. Soc. 99(10) (1952) 369-380.
[25] H.E. Evans, M.P. Taylor, Diffusion Cells and Chemical Failure of MCrAlY Bond Coats in Thermal-Barrier Coating Systems, Oxid. Met. 55(1/2) (2001) 17-34.
[26] B.A. Pint, K.L. More, I.G. Wright, Effect of Quaternary Additions on the Oxidation Behavior of Hf-Doped NiAl, Oxid. Met. 59(3/4) (2003) 257-283.
[27] G. Wang, B. Gleeson, D.L. Douglass, A diffusional analysis of the oxidation of binary multiphase alloys, Oxid. Met. 35(5-6) (1991) 333-348.
[28] F. Ebrahimi, T.G. Hoyle, Brittle-to-ductile transition in polycrystalline NiAl, Acta Mater. 45(10) (1997) 4193-4204.
[29] C. Zhao, Y. Zhou, Z. Zou, L. Luo, X. Zhao, F. Guo, P. Xiao, Effect of

alloyed Lu, Hf and Cr on the oxidation and spallation behavior of NiAl, Corros. Sci.126 (2017) 334-343.
[30] D. Prajitno, B. Gleeson, D.J. Young, The cyclic oxidation behaviour of α-Cr + β-NiAl alloys with and without trace Zr addition, Corros. Sci. 39(4) (1997) 639-654.
[31] M.W. Brumm, H.J. Grabke, The oxidation behaviour of NiAl-I. Phase transformations in the alumina scale during oxidation of NiAl and NiAl-Cr alloys, Corros. Sci. 33(11) (1992) 1677-1690.
[32] T. Gheno, M. Zahiri Azar, A.H. Heuer, B. Gleeson, Reaction morphologies developed by nickel aluminides in type II hot corrosion conditions: The effect of chromium, Corros. Sci.101 (2015) 32-46.
[33] J.A. Nychka, D.R. Clarke, Quantification of Aluminum Outward Diffusion During Oxidation of FeCrAl Alloys, Oxid. Met. 63(5-6) (2005) 325-352.
[34] J. Lu, Y. Chen, C. Zhao, H. Zhang, L. Luo, B. Xu, X. Zhao, F. Guo, P. Xiao, Significantly improving the oxidation and spallation resistance of a MCrAlY alloy by controlling the distribution of yttrium, Corros. Sci.153 (2019) 178-190.
[35] E. Hejrani, D. Sebold, W.J. Nowak, G. Mauer, D. Naumenko, R. Vaßen, W.J. Quadakkers, Isothermal and cyclic oxidation behavior of free standing MCrAlY coatings manufactured by high-velocity atmospheric plasma spraying, Surf. Coat. Technol. 313 (2017) 191-201.
[36] J.W. Hutchinson, M.Y. He, A.G. Evans, The influence of imperfections on the nucleation and propagation of buckling driven delaminations, J. Mech. Phys. Solids 48(4) (2000) 709-734.
[37] R.W. Jackson, D.M. Lipkin, T.M. Pollock, Thermal barrier coating adherence to Hf-modified B2 NiAl bond coatings, Acta Mater. 80 (2014) 39-47.
[38] R.J. Christensen, V.K. Tolpygo, D.R. Clarke, The influence of the reactive element yttrium on the stress in alumina scales formed by oxidation, Acta Mater. 45(4) (1997) 1761-1766.
[39] V.K. Tolpygo, D.R. Clarke, Alumina scale failure resulting from stress relaxation, Surf. Coat. Technol.120-121 (1999) 1-7.
[40] L. Qiu, F. Yang, W. Zhang, X. Zhao, P. Xiao, Effect of Al content on the lifetime of thermally grown oxide formed on Ni–Al alloys after isothermal oxidation, Corros. Sci. 89 (2014) 13-20.
[41] T. Xu, S. Faulhaber, C. Mercer, M. Maloney, A. Evans, Observations and analyses of failure mechanisms in thermal barrier systems with two phase bond coats based on NiCoCrAlY, Acta Mater. 52(6) (2004) 1439-1450.
[42] J. Lu, Y. Chen, H. Zhang, L. He, R. Mu, Z. Shen, X. Zhao, F. Guo, Y/Hf-doped Al0.7CoCrFeNi high-entropy alloy with ultra oxidation and spallation resistance at 1200 °C, Corros. Sci. 174 (2020).
[43] J.L. Smialek, Oxidation Resistance and Critical Sulfur Content of

Single Crystal Superalloys, J. Eng. Gas. Turbines Power 120(2) (1998) 370-374.
[44] D. Naumenko, B.A. Pint, W.J. Quadakkers, Current Thoughts on Reactive Element Effects in Alumina-Forming Systems: In Memory of John Stringer, Oxid. Met. 86(1-2) (2016) 1-43.
[45] H.J. Grabke, D. Wiemer, H. Viefhaus, Segregation of sulfur during growth of oxide scales, Appl. Surf. Sci. 47(3) (1991) 243-250.
[46] Y. Jiang, J.R. Smith, A.G. Evans, First principles assessment of metal/oxide interface adhesion, Appl. Phys. Lett. 92(14) (2008) 141918.
[47] Z. Wěiss, K. Marshall, Elemental depth profiling of coated and surface-modified materials by GD-OES: hard coatings on cutting tools, Thin Solid Films 308-309 (1997) 382-388.
[48] A. Gil, D. Naumenko, R. Vassen, J. Toscano, M. Subanovic, L. Singheiser, W.J. Quadakkers, Y-rich oxide distribution in plasma sprayed MCrAlY-coatings studied by SEM with a cathodoluminescence detector and Raman spectroscopy, Surf. Coat. Technol. 204(4) (2009) 531-538.

Figures Captions

Fig. 1 Structure analysis of EHEA: (a, b) a low magnification BSE image and (b) a locally amplifying BSE image of the region marked in (a), showing the typical eutectic structure composed of γ' and β phases; (c) A high-angle annular dark-field (HAADF) STEM image and (d) the corresponding elemental maps, showing the elemental distribution in γ' and β phases.

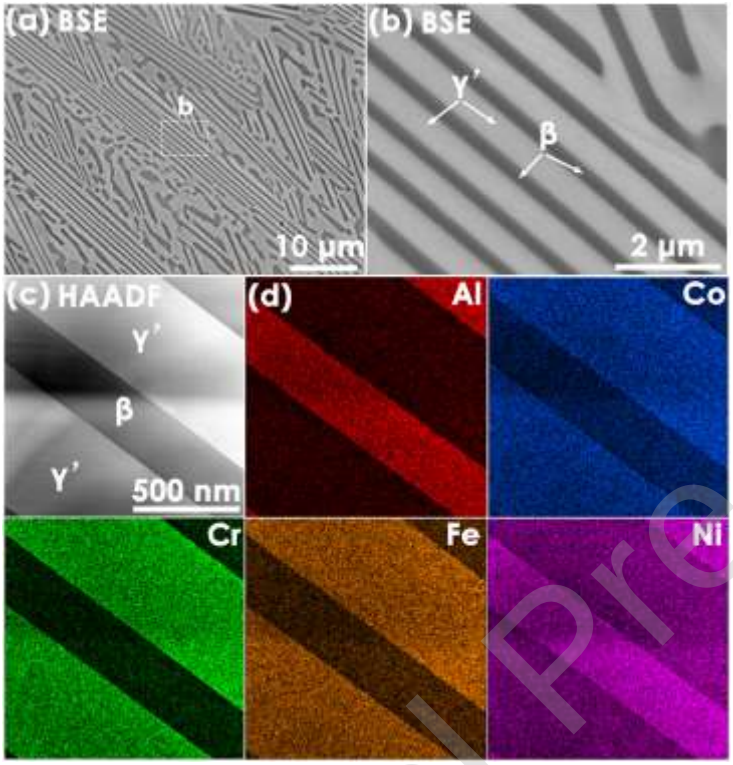

Fig. 2 Surface and cross-sectional morphology of the EHEA after cyclic oxidation: (a, d) low magnification BSE images and (a1, d1) locally amplifying BSE images, showing the well intact Al_2O_3 scale and detailed grain structure of Al_2O_3 scale after 1008 h oxidation at 1100 °C and 1200 °C, respectively; (b, e) low magnification BSE images and (c, f) locally amplifying BSE images with SEM-EDX maps, showing the homogeneous and continuous Al_2O_3 formation after 1008 h oxidation at 1100 °C and 1200 °C, respectively; (g) A high magnification SEM image of fractural surface for Al_2O_3 scale, showing the columnar grain structure.

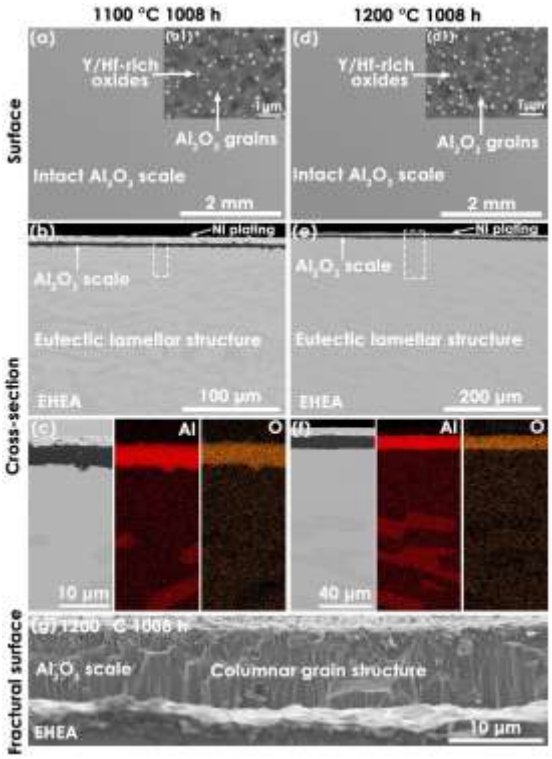

Fig. 3 Surface and cross-sectional morphology of the CNA after cyclic oxidation: (a, b) low magnification BSE images, showing the spalled surface and interface of Al_2O_3 scale after 720 h oxidation at 1100 °C; (c, d) low magnification BSE images and (c1) locally amplifying BSE images of (c), showing the spalled surface and interface of Al_2O_3 scale and phase constitutions of interfacial imperfections after 504 h oxidation at 1200 °C; (e) A high magnification SEM image of fractural surface for Al_2O_3 scale, showing the columnar grain structure. (Once the ratio of scale spallation during the cyclic oxidation exceeds 15%, this oxidation time is defined as the time of scale failure and the cyclic oxidation test will be stopped.)

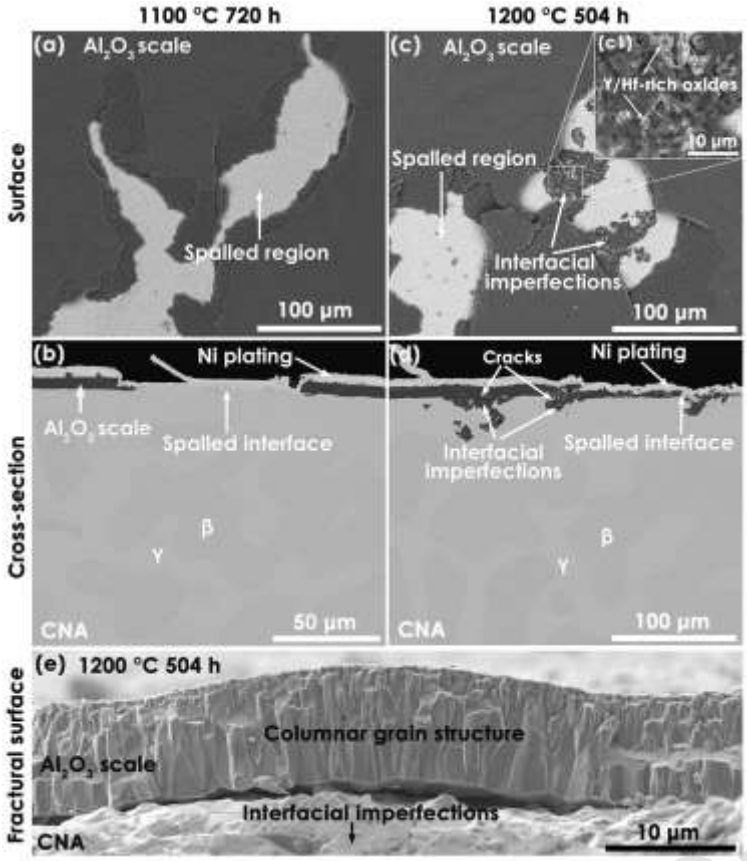

Fig. 4 Evolution of Al_2O_3 scale thickness as a function of the oxidation time at 1100 °C and 1200 °C for the EHEA and CNA. (The Al_2O_3 scale thickness is measured through the ratio of cross-sectional area of the scale to the length of interface in a single BSE image with a magnification of 5000 ×. Each point in this image represents the average value of 5 measurements obtained from five separate BSE images. The Al_2O_3 scale thickness is only measured at these regions away from the interfacial imperfections for the oxidized CNA at 1200 °C.)

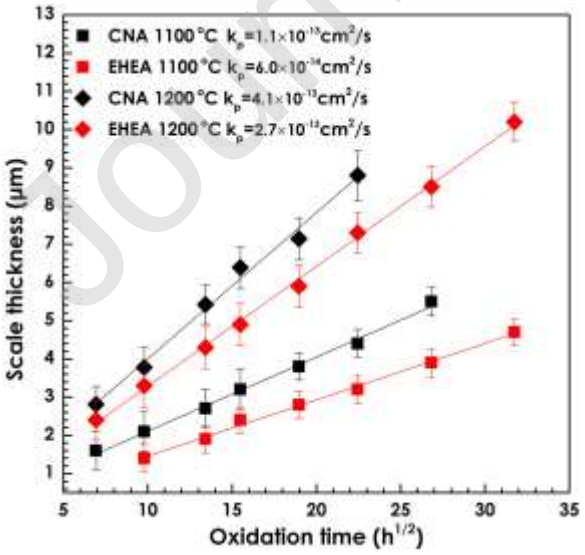

Fig. 5 (a) Evolution of residual stress in the Al_2O_3 scale as a function of oxidation time for the EHEA and the CNA at 1100 °C and 1200 °C; (b) peak shift of R2 line collected from the Al_2O_3 scale and the stress-free sapphire was utilized to be as stress reference. (The average residual stress is obtained by the average value of 50 measurements. The error bar is the standard deviation of 50 measurements.)

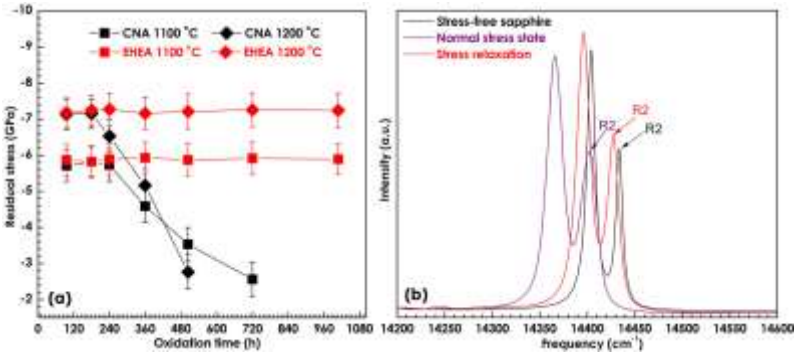

Fig. 6 Quantitative depth profiles of corresponding elements for the EHEA after oxidation for 1008 h at 1200 °C. S*100 represents that the actual S concentration is 100-times lower than the value presented in this figure.

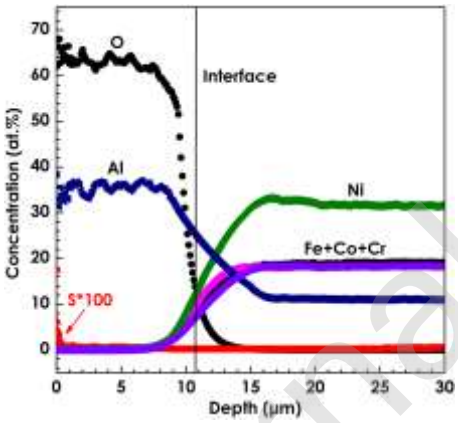

Fig. 7 A schematic diagram, representing the evolution of driving force for scale delamination (solid lines) and interfacial toughness (dash lines) as a function of the oxidation time for two alloys. The black lines represent the CNA and red lines represent the EHEA. Line A-D are 1100 °C and line E-H are 1200 °C.